Electronic Supplementary Material (ESI) for Catalysis Science & Technology.

Electronic Supplementary Information

Design of Ruthenium/Iron Oxide Nanoparticle Mixtures for Hydrogenation of Nitrobenzene to Aniline: Catalytic Behavior Influenced by Iron Oxide Nanoparticles

Rosemary Easterday, Olivia Sanchez-Felix, Yaroslav Losovyj, Maren Pink, Barry D. Stein, David Gene Morgan, Mikhail Rakitin, Valentin Yu. Doluda, Mikhail G. Sulman, W. E. Mahmoud, A. A. Al-Ghamdi, Lyudmila M. Bronstein

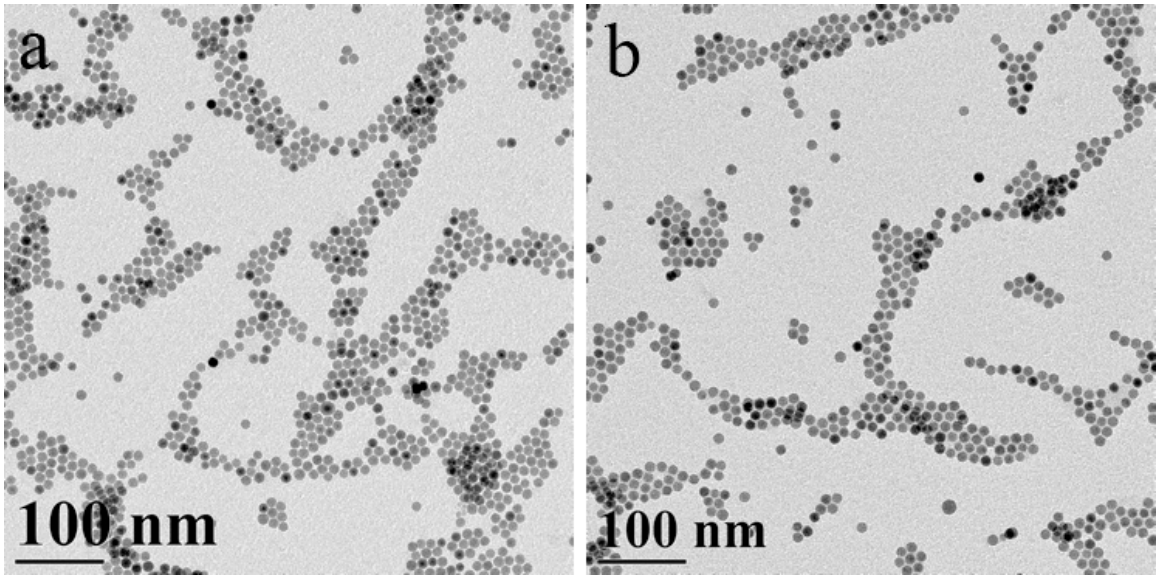

Figure S1. As-synthesized 8.2 nm FeO-Fe_3O_4 (a) and the NPs after oxidation (8.1 nm).

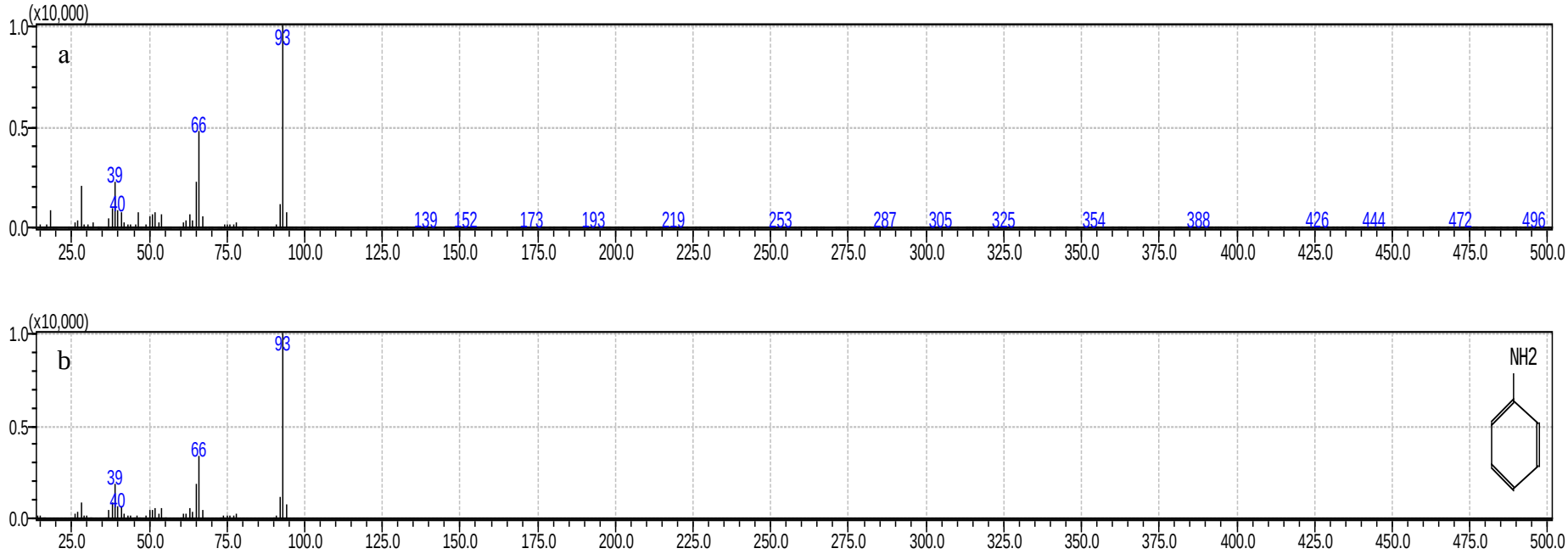

Figure S2. (a) Mass spectrum of the reaction mixture after the experiment with Ru-14 in the following reaction conditions: T = 150°C, C_0 = 0.06 μM, C_c = 3g/L. (b) NIST library spectrum of aniline.

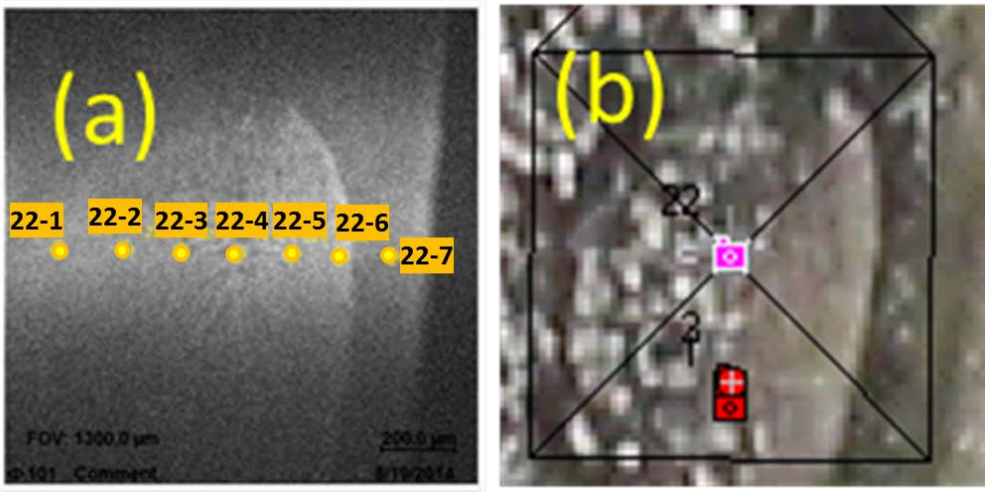

Figure S3. (a) SXI image of the 8.1 nm iron oxide NP sample drop cast onto the native surface of a Si(111) wafer, 1300 µm × 1300 µm FOV. (b) Optical image. High resolution Fe 3p XPS spectra were taken from each spot labelled (a).

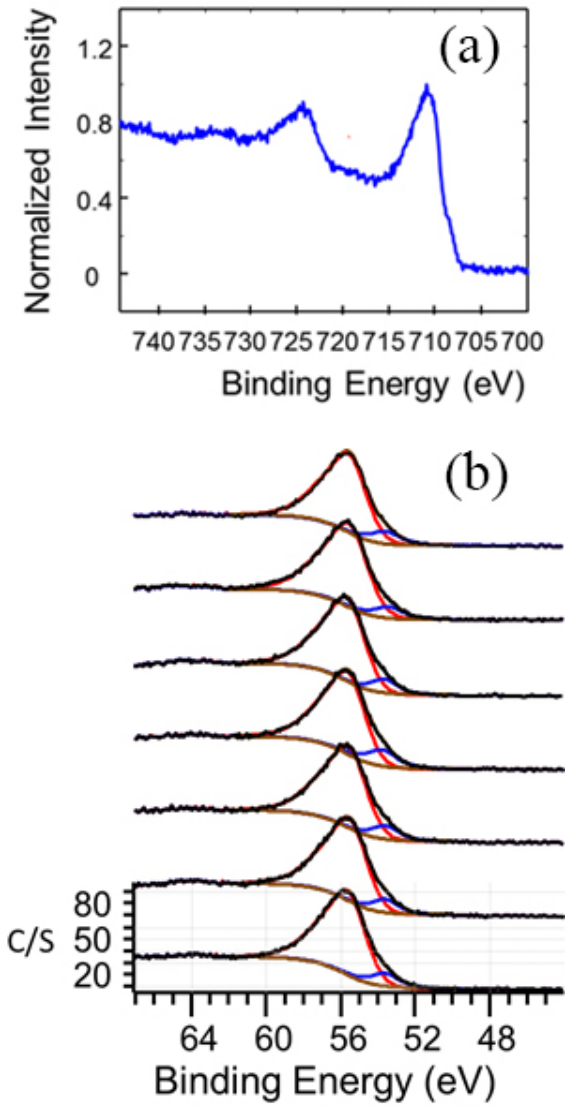

Figure S4. High resolution Fe 2p (a) and Fe 3p (b) XPS spectra. The Fe 3p spectra in (b) correspond to the spots labelled in Figure S2a from the bottom to the top: 22-1, 22-2, 22-3, 22-4, 22-5, 22-6, 22-7. The Fe^{2+} component is represented by blue color and the Fe^{3+} component is shown by red color for all spots.

The 8.1 nm NPs exhibit the typical spectrum shape for the Fe 2p region consistent with that of pure bulk Fe_2O_3[1, 2] with a weak satellite structure at 718.9 eV BE (Fig. S3a) in the Fe $2p_{3/2}$ region. For the bulk samples containing largely Fe^{2+} ions, this satellite appears at about 4 eV BE lower (714. 7).[1] On the other hand, the absence of any pronounced satellite structure in the Fe $2p_{3/2}$ region is the signature of Fe_3O_4 with a stoichiometric ratio between the 2+ and 3+ iron ions.[1] The data obtained for the Fe 3p region are summarized in the Table S1.

Table S1. Binding energies and the Fe^{2+}/ Fe^{3+} peak ratios for the spots labelled in the Figure S2a.

See Fig. S2 for labels	Component Fe^{2+}, at %	Component Fe^{3+}, at %	BE Fe^{2+}, eV	BE Fe^{3+}, eV	Fe^{2+}/ Fe^{3+} ratio
22-1	12.857	87.143	53.65	55.67	0.147
22-2	12.57	87.430	53.60	55.56	0.144
22-3	13.179	86.821	53.59	55.6	0.152
22-4	16.799	83.201	53.77	55.65	0.202
22-5	12.706	87.294	53.67	55.69	0.146
22-6	10.370	89.630	53.44	55.60	0.116
22-7	12.939	87.061	53.61	55.61	0.149
Average	13.06	86.94	53.62	55.63	0.151
Standard deviation	1.89	1.89	0.099	0.046	0.0256

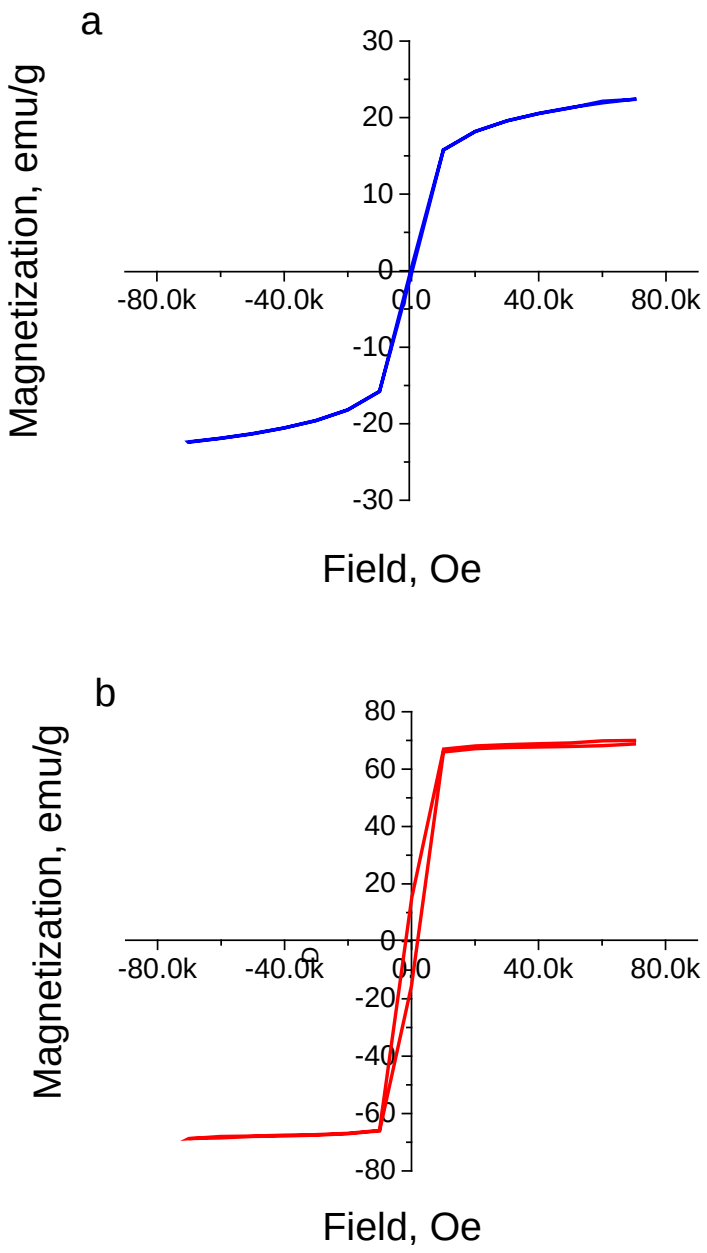

Figure S5. Hysteresis curves at 300 K for 22.3 nm FeO-Fe_3O_4 NPs (a) and 22.1 nm Fe_3O_4/γ-Fe_2O_3 (b). The presence of hysteresis in (b) demonstrates that after oxidation the iron oxide NPs are ferrimagnetic at room temperature.

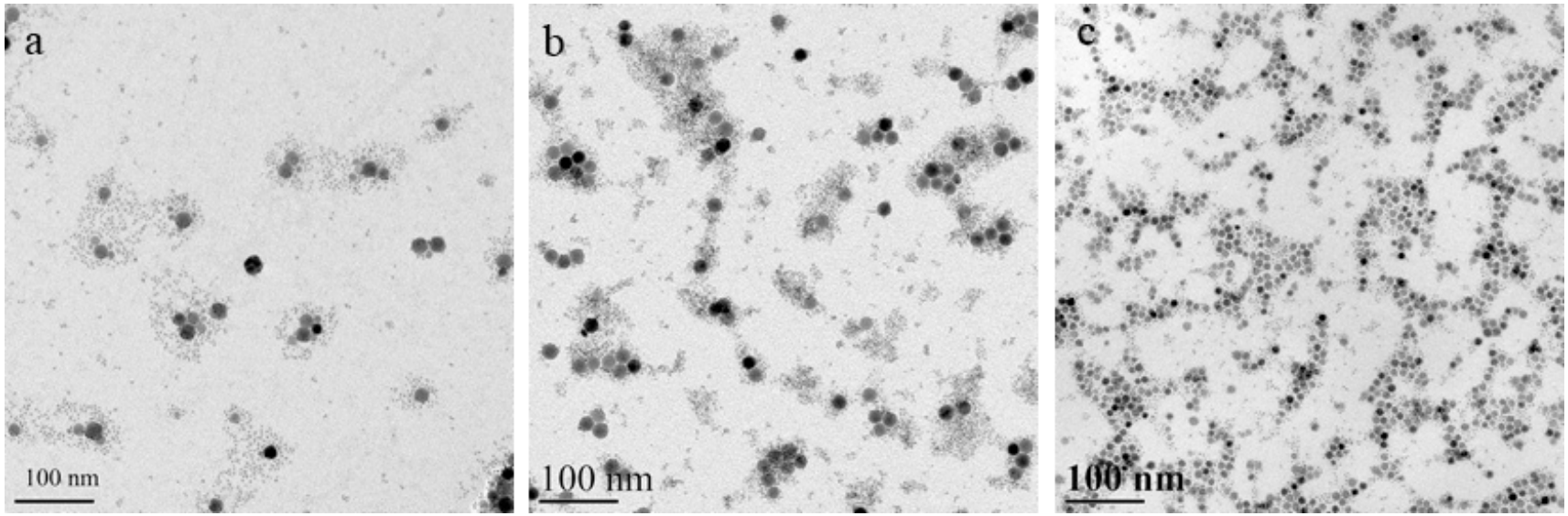

Figure S6. TEM images of Ru-12 (a), Ru-14 (b), and Ru-6 (c).

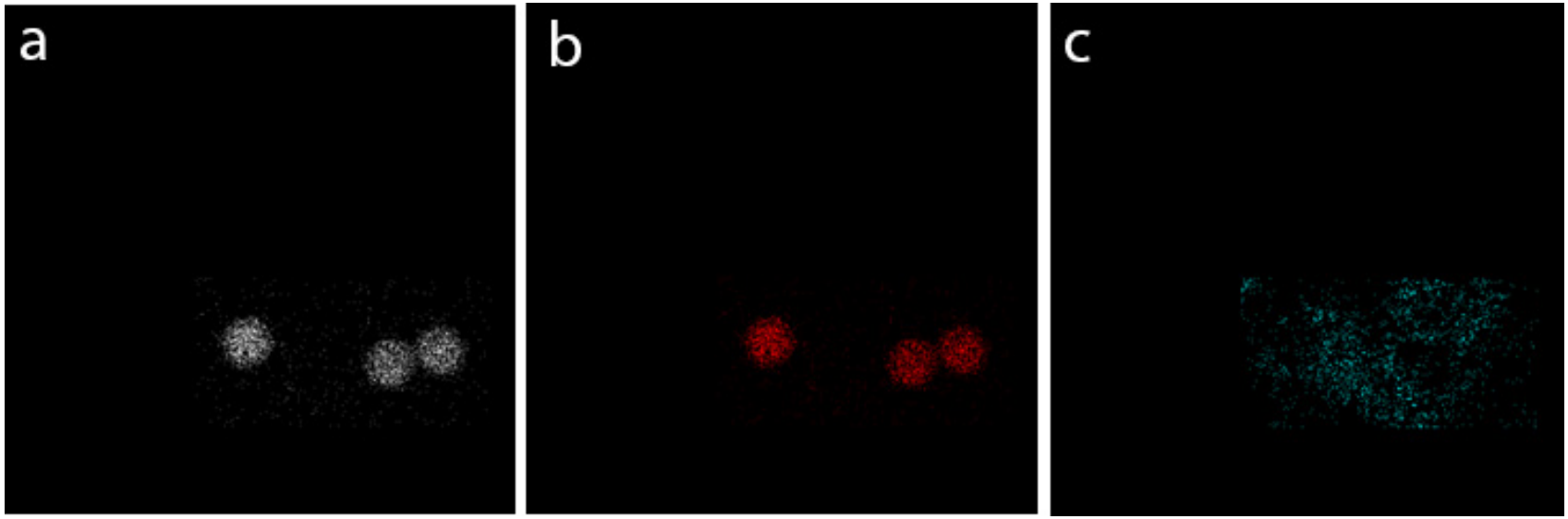

Figure S7. Dark-field STEM image (a) and Fe (b) and Ru (c) maps obtained by STEM EDS for Ru-14. The Ru map shows only a noise similar to that of xenon absent in the sample. Other elements present in the spectrum are consistent with either the sample holder or the copper TEM grid.

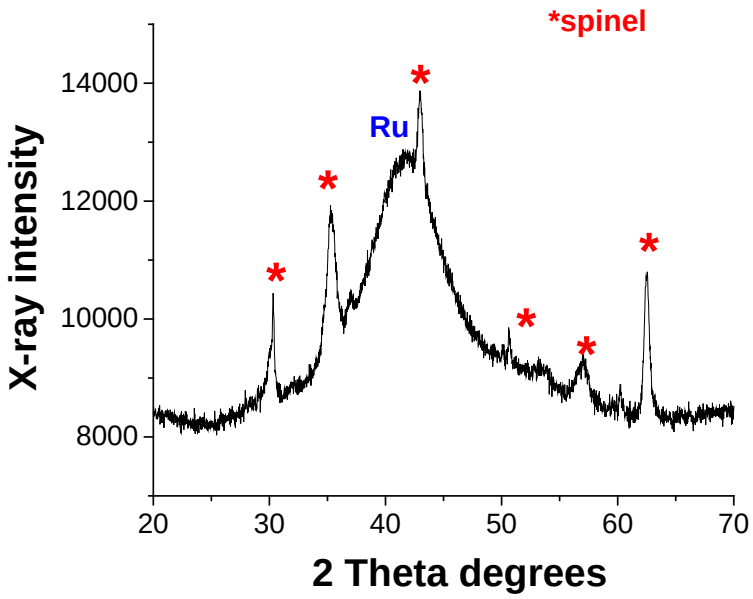

Figure S8. XRD pattern of Ru-14.

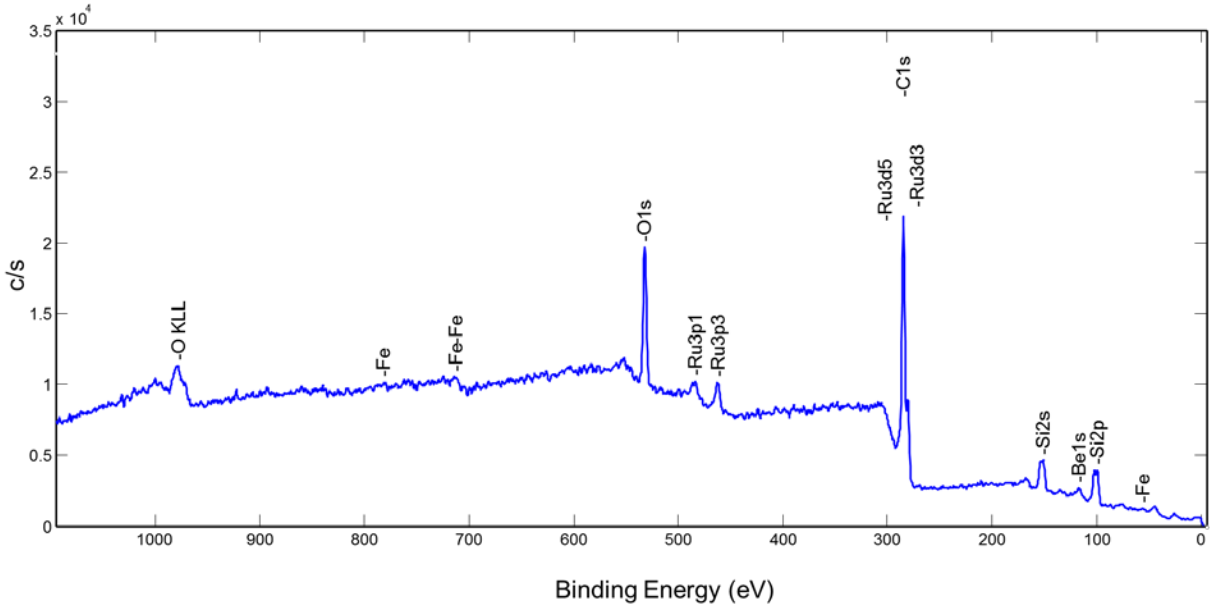

Figure S9. The survey spectrum of Ru-14 drop cast on the native surface of a Si(111) wafer.

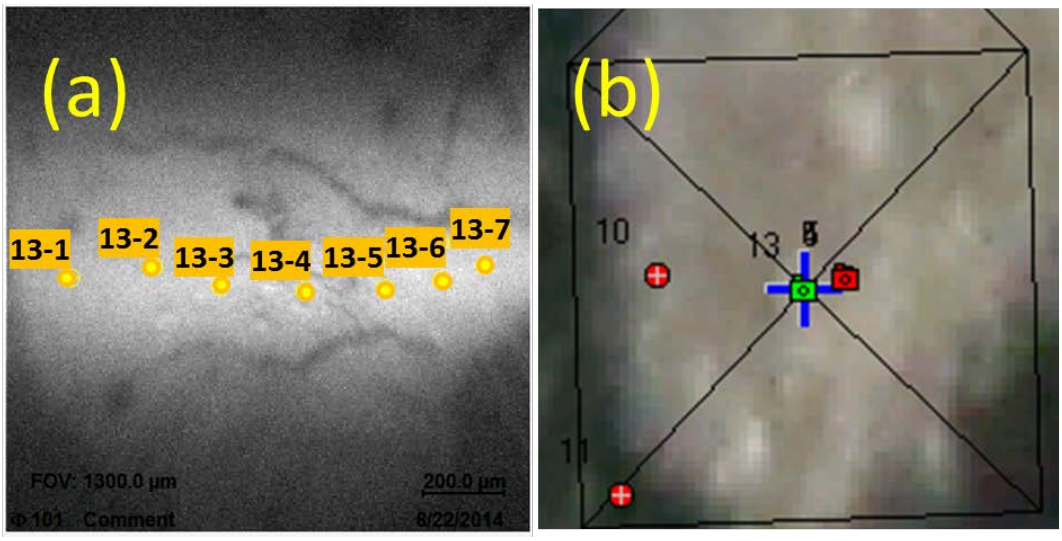

Figure S10. (a) SXI image of Ru-14 drop cast onto the native surface of a Si(111) wafer, 1300 µm × 1300 µm FOV. (b) Optical image. High resolution Fe 3p XPS spectra were taken from each spot labelled at (a).

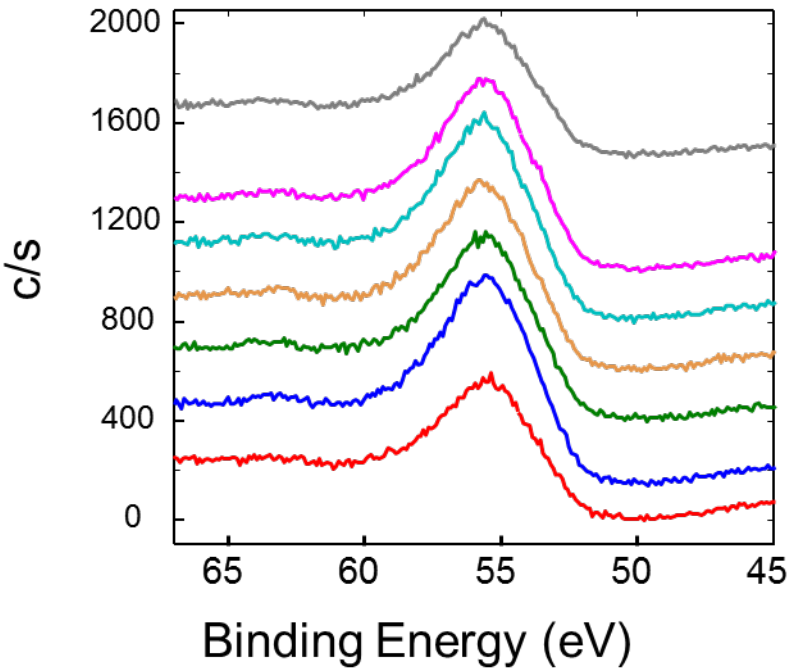

Figure S11. High resolution Fe 3p XPS spectra of Ru-14 drop cast onto the native surface of a Si(111) wafer. Spectra taken from the bottom to the top for the spots 13-1, 13-2, 13-3, 13-4, 13-5, 13-6, and 13-7 as labelled in Figure S9a.

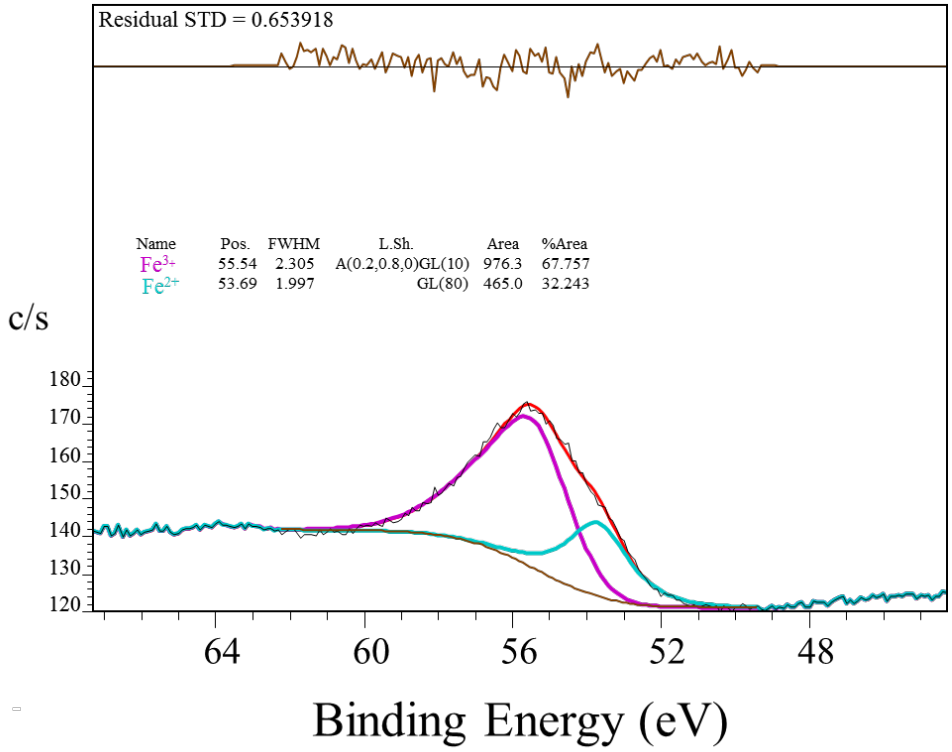

Figure S12. High resolution Fe 3p XPS spectrum of Ru-14 for the spot labeled 13-7. The Fe^{2+} component is represented in blue and the Fe^{3+} component in red .

Table S2. Binding energies and the Fe^{2+}/ Fe^{3+} peak ratios for the spots labelled in the Figure S9a.

See Fig. S9 for labels	Component Fe^{2+}, at %	Component Fe^{3+}, at %	BE Fe^{2+}, eV	BE Fe^{3+}, eV	Fe^{2+}/ Fe^{3+} ratio
13-1	26.825	73.148	53.55	55.42	0.367
13-2	37.217	62.783	53.88	55.64	0.593
13-3	30.064	69.963	53.7	55.53	0.429
13-4	31.376	68.624	53.82	55.63	0.457
13-5	34.855	65.145	53.84	55.63	0.535
13-6	29.683	70.317	53.66	55.52	0.422
13-7	23.243	67.757	53.69	55.54	0.476
Average	31.75	68.25	53.73	55.56	0.468
Standard deviation	3.45	3.445	0.117	0.075	0.075

Table S3. Parameters of the XPS spectrum for Ru-14 deconvolution in the Ru 3p and 4p regions.

Transition	Position, eV	PosSep, eV	FWHM, eV	%Gauss	%Area	ChiSquared
Ru 3p	461.41	0.00	3.14	80	63.35	2.45
	463.16	1.74	3.64	80	36.65	
Ru 4p	43.52	0.00	2.85	100	60.03	1.28
	46.38	2.86	3.10	80	39.97	

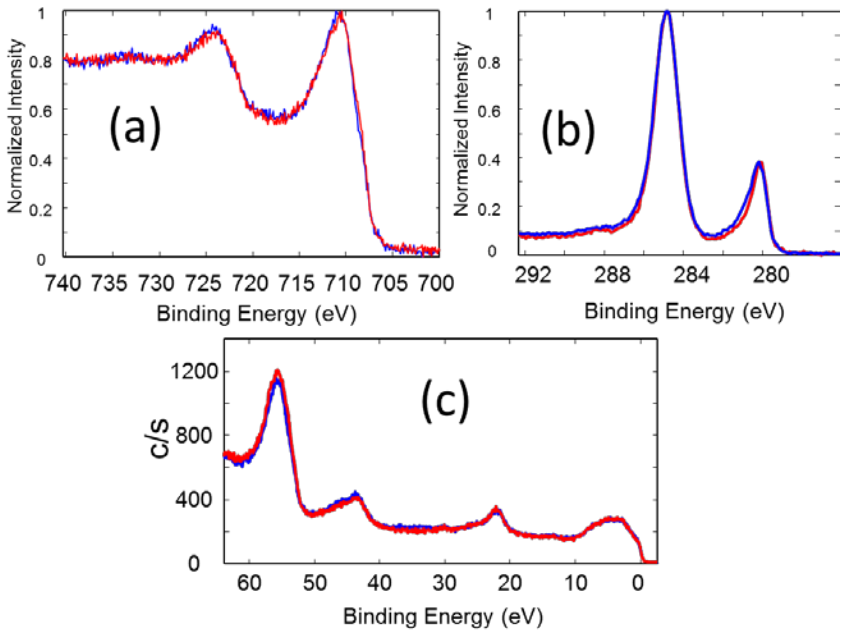

Figure S13. High resolution spectra Fe 3p (a), Ru 3d (b) and the valence band region (c) of Ru-14 before (blue) and after (red) 1 min 1 kV cycle of argon sputtering.

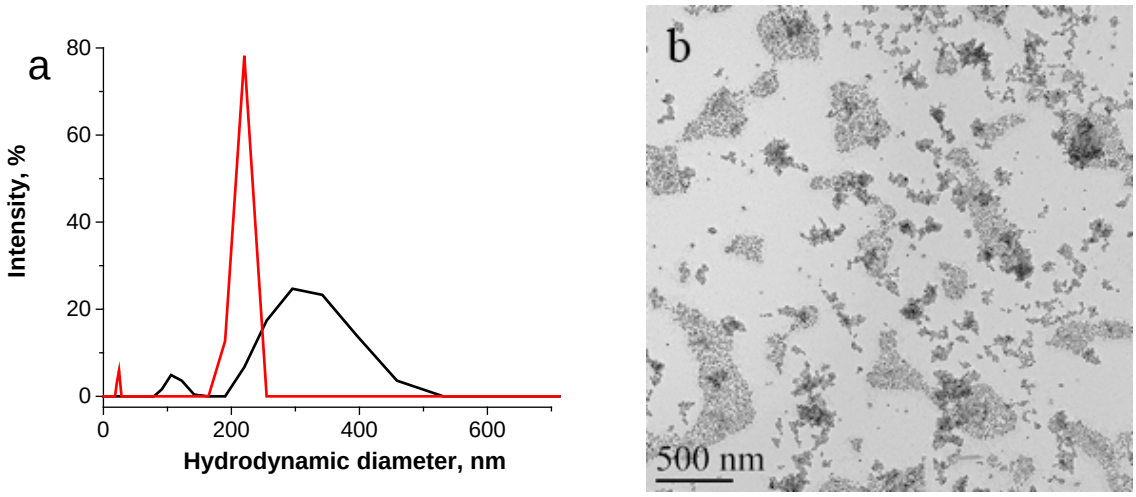

Figure S14. DLS intensity distributions vs. hydrodynamic diameter (a) of Ru-7 (black) and Ru-8 (red) and the TEM image of the latter (b).

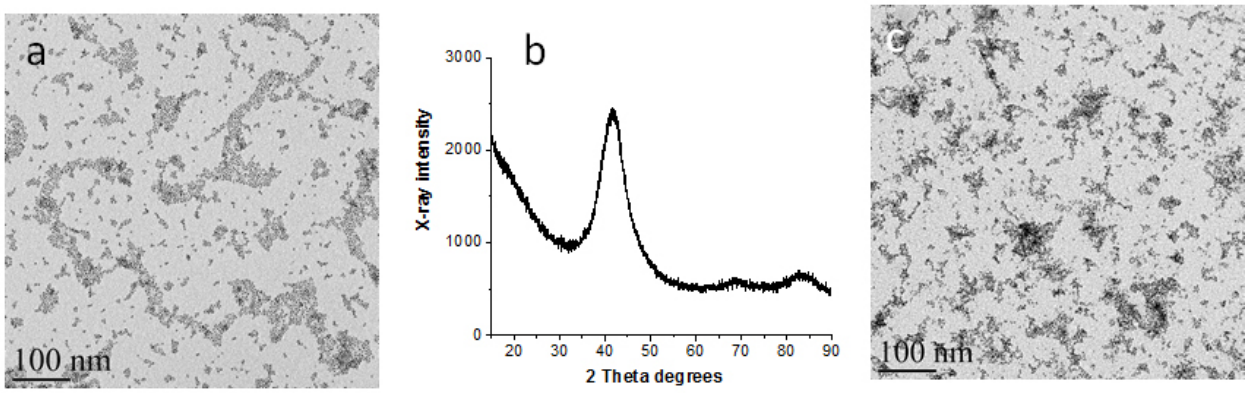

Figure S15. TEM image (a) and XRD pattern (b) of Ru-17 and the TEM image of Ru-18.

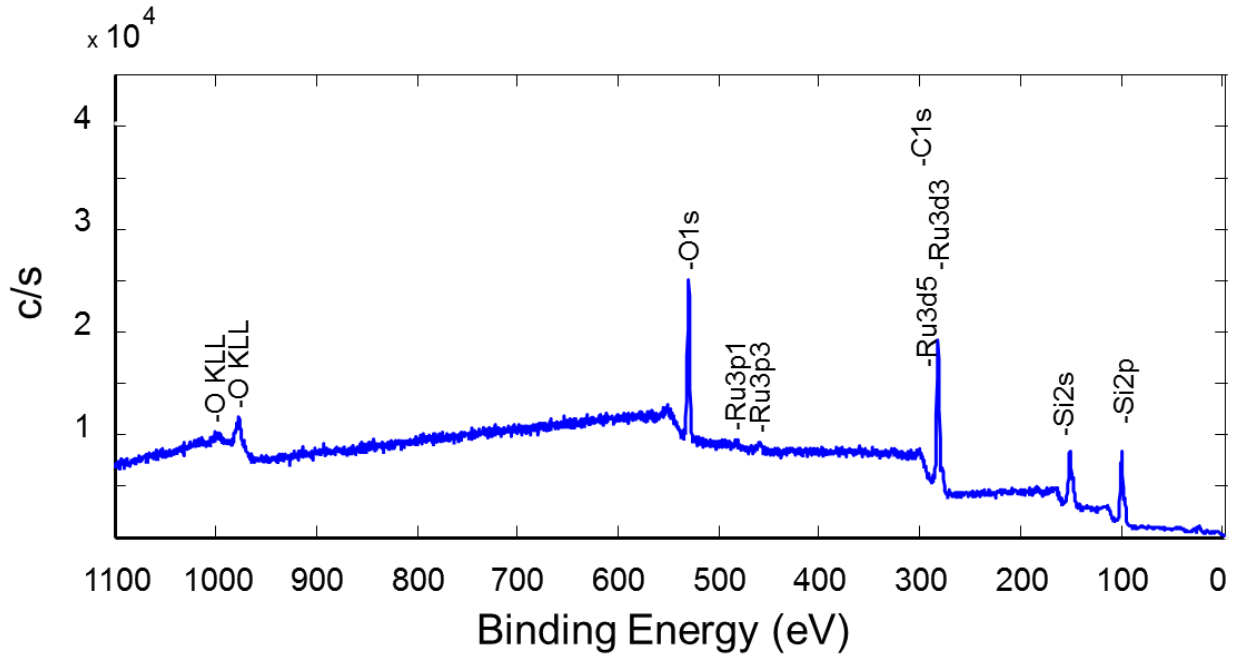

Figure S16. A typical survey spectrum of Ru-17 drop cast on the native surface of a Si(111) wafer.

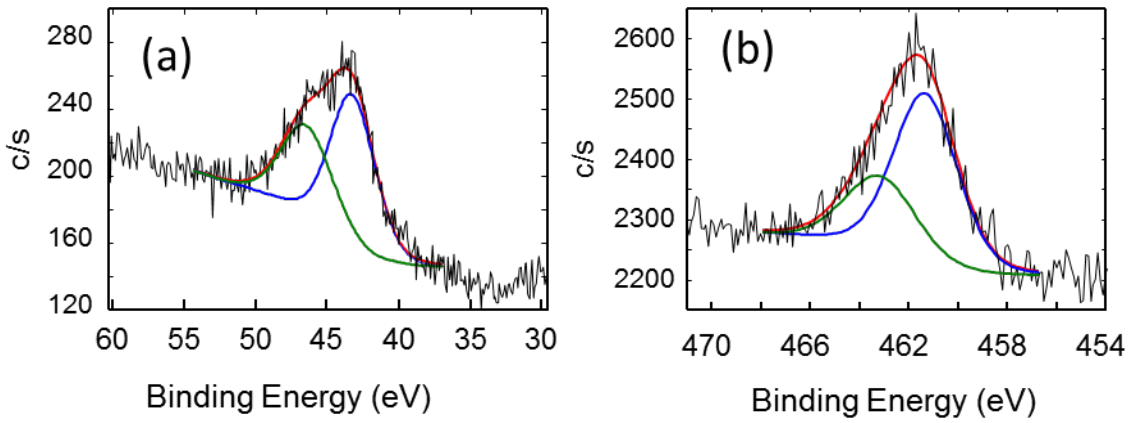

Figure S17. High resolution Ru 4p (a) and 3p (b) XPS of Ru-17 with deconvolution. See Table S4 for fitting parameters.

Table S4. Parameters of the XPS spectrum for Ru-17 deconvolution in the Ru 3p and 4p regions.

Transition	Position, eV	PosSep, eV	FWHM, eV	%Gauss	%Area	ChiSquared
Ru 3p	461.31	0.00	3.05	80	67.52	1.29
	463.16	1.85	3.40	80	32.48	
Ru 4p	43.26	0.00	3.69	80	59.60	1.28
	46.45	3.19	4.18	80	40.40	

High resolution spectra for the Fe 2p region reveal no detectable iron photo yield before (red) and after (blue) a 0.5 min 4.0 kV argon sputtering cycle, which suggests that the absence of the Fe signal is not related to suppression of iron photo yields by the presence of surface contamination on the NP (see Fig. S17a). It is worth noting that Ru NPs are exceptionally stable with respect to argon sputtering compared to PtFe NPs reported by us earlier,[3] which can be assigned to stronger stabilization by surfactants. Indeed, there is no noticeable removal of carbon and/or nitrogen signatures in the range of their 2p transitions (10-20 eV binding energies) upon argon bombardment up to 1 kVe of ion energy (cyan spectrum, Fig. S17b). As valence band carbon and nitrogen 2p features vanish and the oxygen 2s signal diminishes upon more intense sputtering, the Ru 4p intensity slightly increases. Notice that the binding energies remain unchanged during sputtering process.

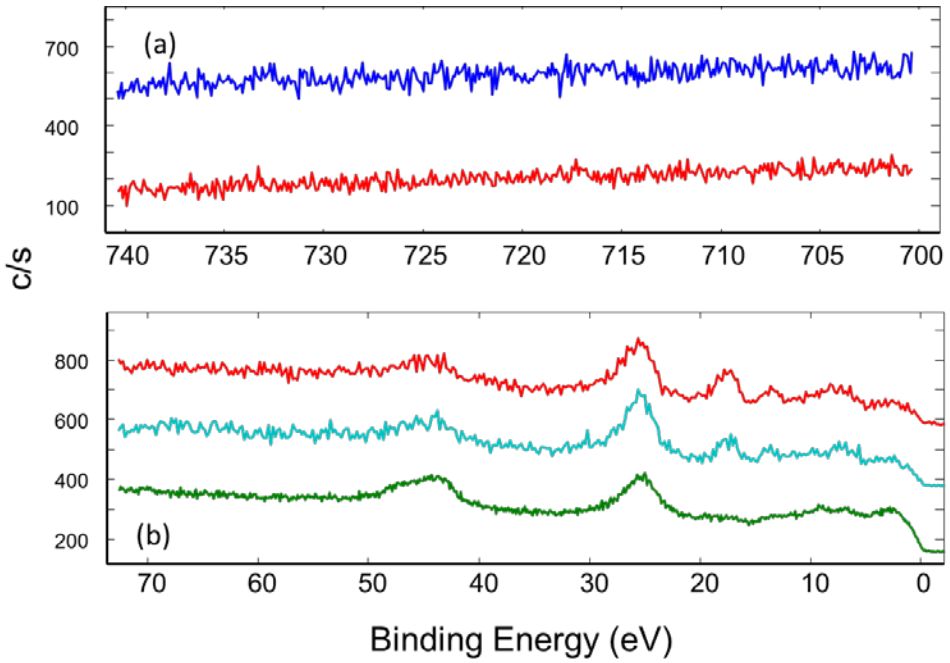

Figure S18. (a) Fe 2p high resolution XPS spectra of Ru-17. The top (blue) spectrum corresponds to the as-inserted sample. The bottom (red) spectrum corresponds to the one cycle (0.5 min) of argon (4 kV) sputtering. (b) High resolution valence band spectra. From the top to the bottom: as-inserted sample (red), middle (cyan) for one cycle (0.5 min) of argon (1 kV) sputtering, bottom (green) for one cycle (0.5 min) of argon (4 kV) sputtering.

Similar changes related to the surface contamination removal upon argon ion bombardment in the C 1s, O 1s and Ru 3p and 3d regions were also observed near the Fermi level region (Fig. S18). As the carbon and oxygen intensities are significantly reduced, there is only a slight increase of the Ru 3d intensity, which might be related to a negligible suppression of the ruthenium related photoemission by carbon and oxygen present on the surface of the fresh sample. This is consistent with corresponding changes in the Ru 4p region.

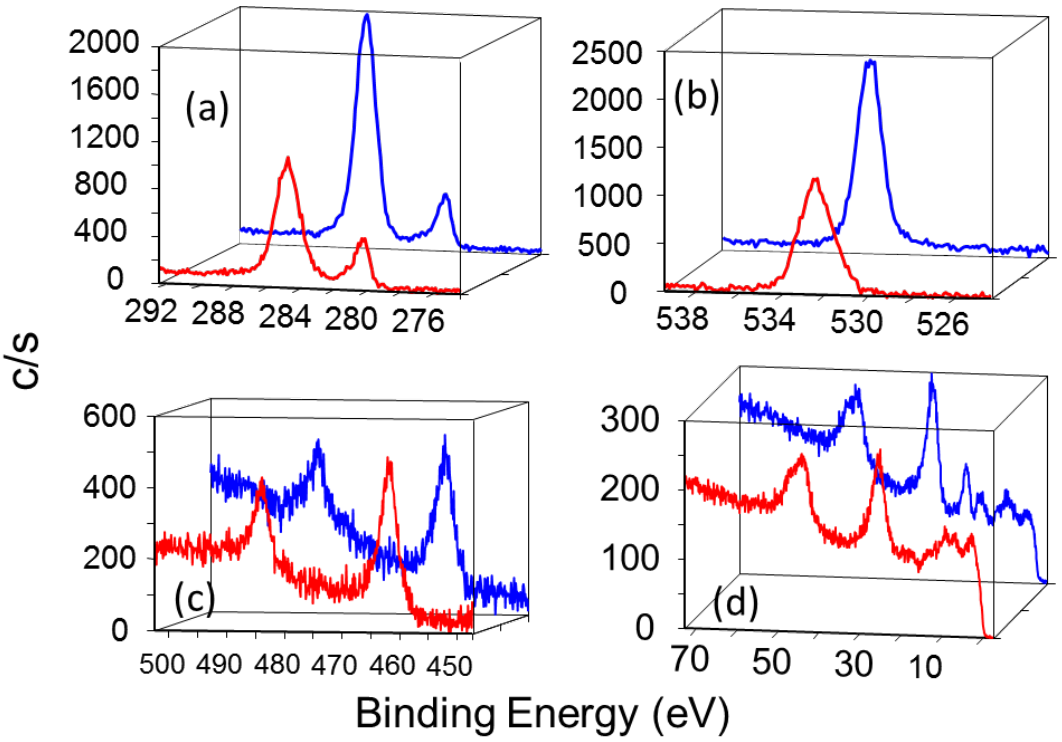

Figure S19. Ru 3d and C 1s (a), O 1s (b), Ru 3p (c) and valence band (d) high resolution XPS spectra of Ru-17 drop cast on the native surface of a Si(111) wafer. Blue spectra correspond to the as-inserted sample, while red spectra were recorded after one cycle (0.5 min) of argon (4 kV) sputtering.

Unlike Ru 3d and 4p, the Ru 4d region near the Fermi level region (about 2 eV BE) exhibits a significant intensity increase (about by a factor of 2) after the two sputtering cycles due to extreme surface sensitivity of the photoemission from that region (Figs. S19d and S20).

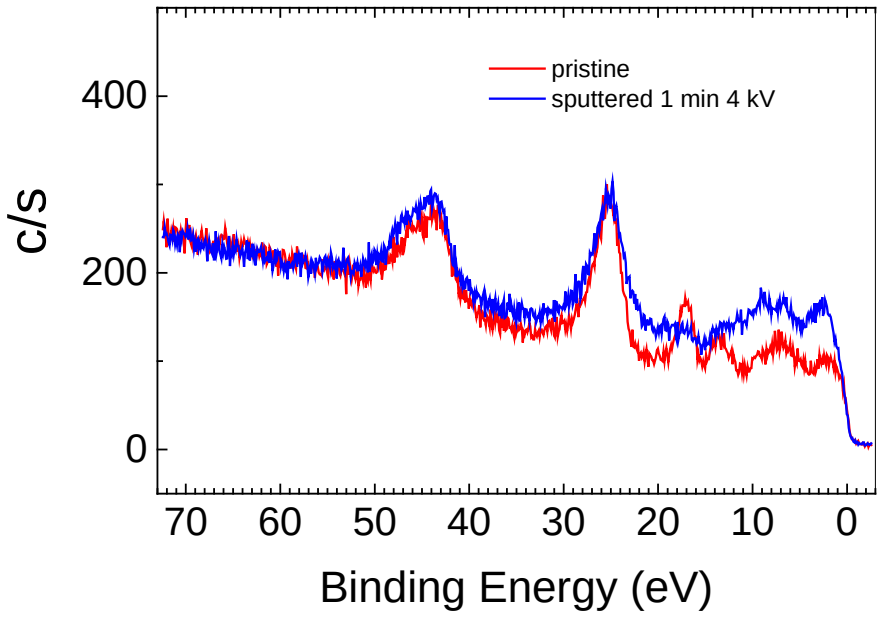

Figure S20. The valence band HR XPS spectra of Ru-17 normalized to the high binding energy side of the Ru 4p peak. The red line is for the as-inserted sample, while the blue spectrum is for the sample after two sputtering cycles at 4 kV argon ions.

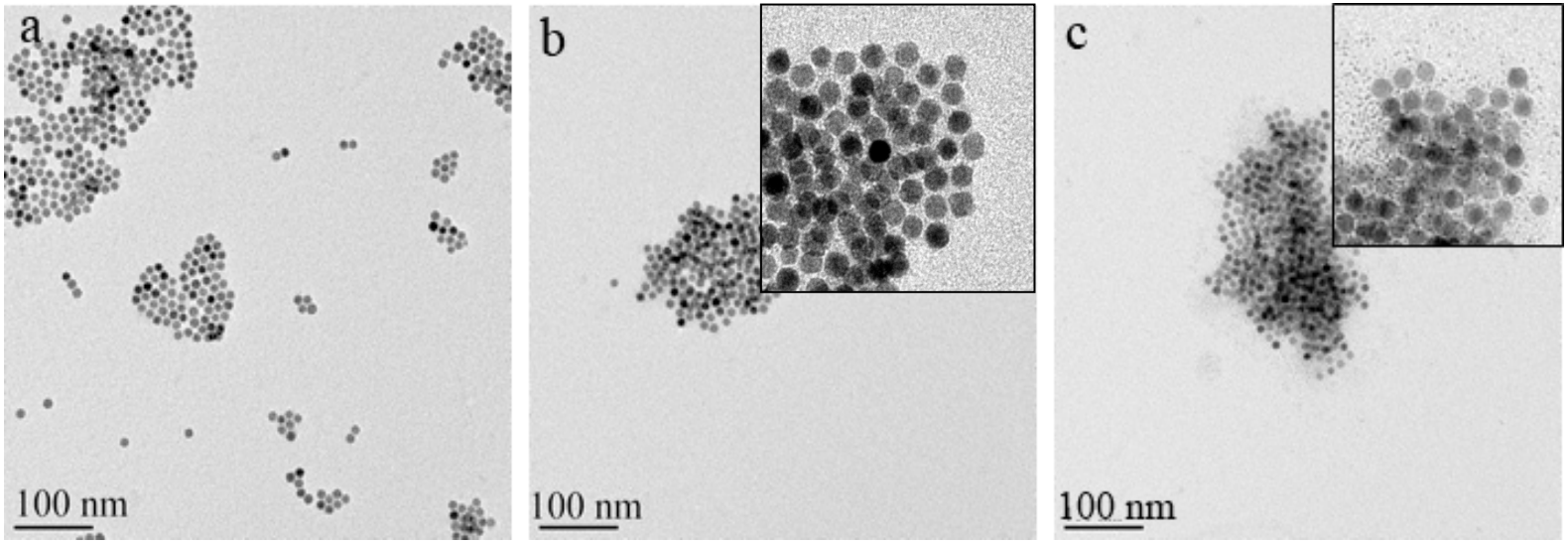

Figure S21. TEM images of specimens taken out of the reaction solution 5 (a), 15 (b), and 25 (c) minutes after $Ru(acac)_3$ injection in the conditions of Ru-7 (Fig. 2). Insets in (b) and (c) show higher magnification images.

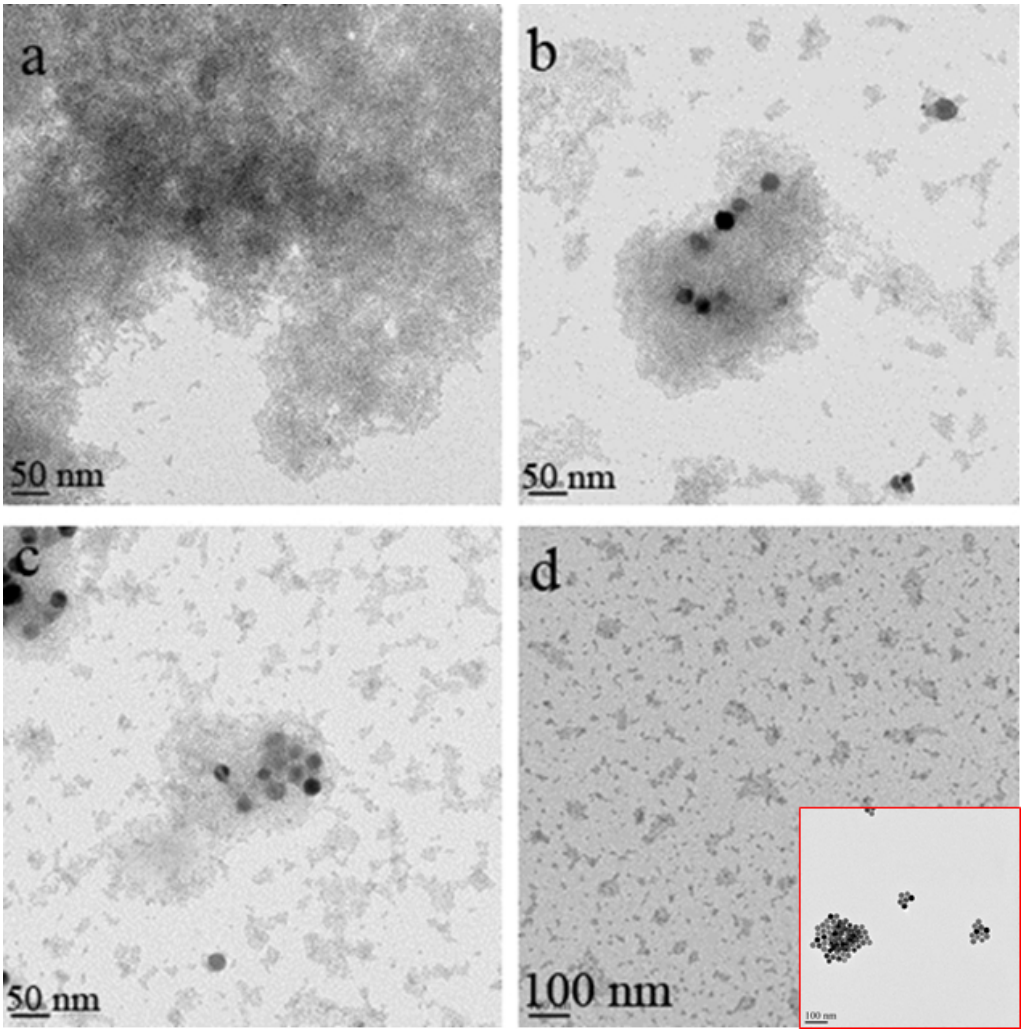

Figure S22. TEM images of the specimens taken out of the reaction solution of Ru-9 5 (a), 15 (b), and 25 (c) minutes after $Ru(acac)_3$ injection. The image in (d) shows a final product after 45 min. Reaction conditions: dioctyl ether, 250 °C, 22.3 nm Fe_3O_4/γ-Fe_2O_3 NPs. Inset in (d) shows the 22.3 nm Fe_3O_4/γ-Fe_2O_3 NPs after heating in diphenyl ether at 250 °C.

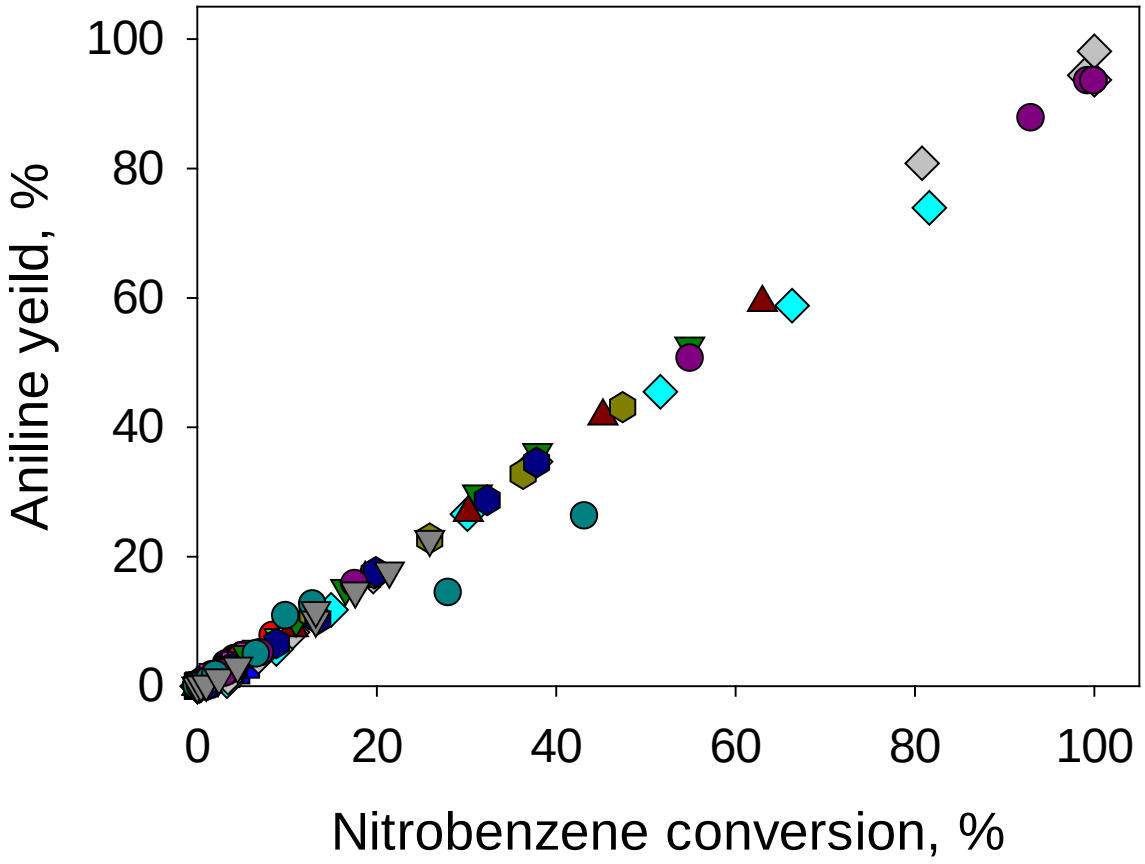

Figure S23. Dependences of the aniline yield on the nitrobenzene conversion at different reaction conditions:

● T = 150°C, C_0 = 0.12 μM, C_c = 3g/L; ● T = 150°C, C_0 = 0.24 μM, C_c = 3g/L; ▼ T = 150°C, C_0 = 0.30 μM, C_c = 3 g/L; ▲ T = 150°C, C_0 = 0.40 μM, C_c = 3g/L; ■ T = 120°C, C_0 = 0.06 μM, C_c = 3g/L; ■ T = 130°C, C_0 = 0.06 μM, C_c = 3 g/L; ◆ T = 140°C, C_0 = 0.06 μM, C_c = 3 g/L; ◆ T = 150°C, C_0 = 0.06 μM, C_c = 3g/L; ▲ T = 160°C, C_0 = 0.06 μM, C_c = 3 g/L; ▼ T = 170°C, C_0 = 0.06 μM, C_c = 3 g/L; ⬢ T = 180°C, C_0 = 0.06 μM, C_c = 3 g/L; ⬢ T = 150°C, C_0 = 0.06 μM, C_c = 2g/L; ● T = 120°C, C_0 = 0.06 μM, C_c = 4g/L; ● T = 120°C, C_0 = 0.06 μM, C_c = 5 g/L; ▼ T = 120°C, C_0 = 0.06 μM, C_c = 6 g/L.

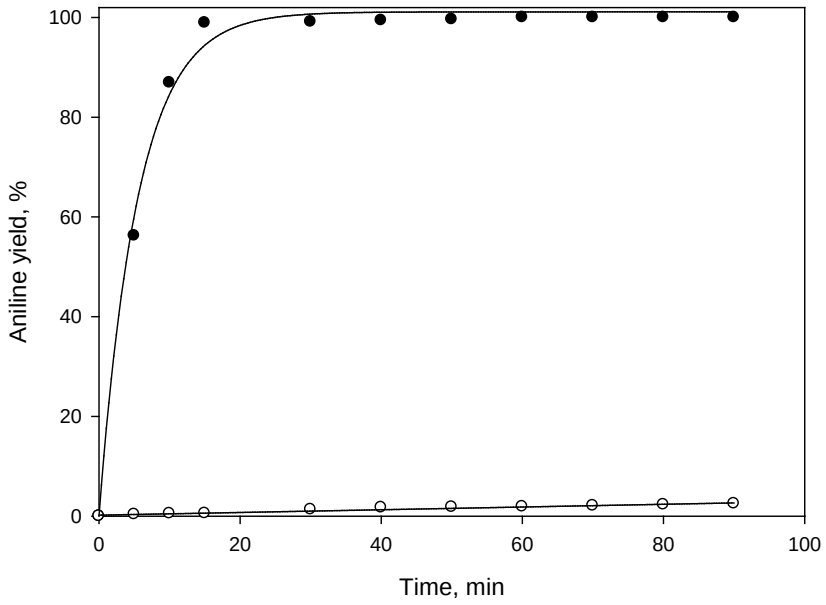

Figure S24. Dependences of the aniline yield on time for Ru-14 (filled circles) and the FeO/Fe_3O_4 NPs (open circles) in the following reaction conditions: T = 150°C, C_0 = 0.06 μM, C_c = 3g/L.

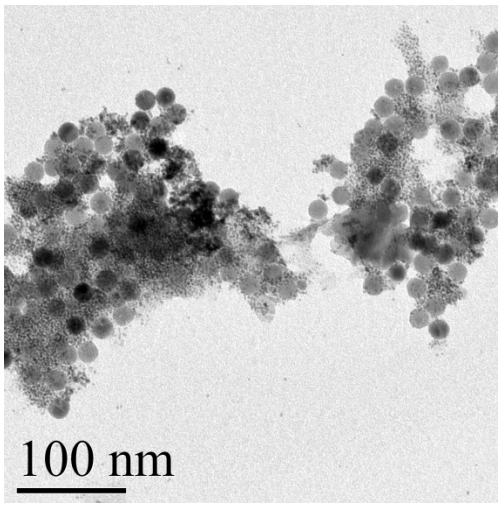

Figure S25. TEM image of Ru-14 after the catalytic reaction.

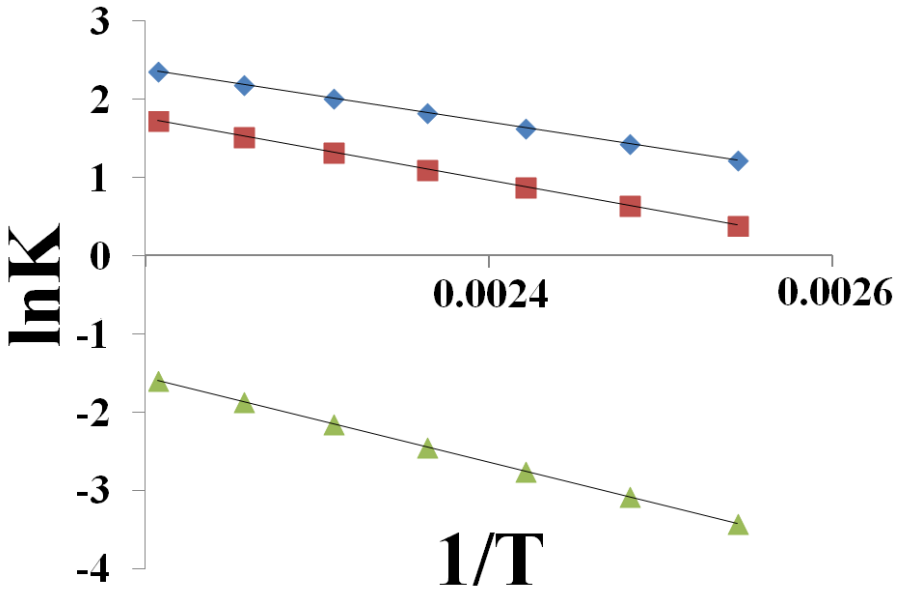

Figure S26. Arrhenius plots for determination of the apparent activation energy for Ru-5 (blue diamonds, y = -3367x + 9.79), Ru-12 (red squares, y = -3969x + 10.49), and Ru-14 (green triangles, y = -5412x + 10.35). Reaction conditions: C_C= 3 g/L; Co = 0.06 µM, P=30 bar, t=120-180 °C.

References

1. Yamashita, T.; Hayes, P. *Applied Surface Science* **2008,** 254, (8), 2441-2449.
2. Muhler, M.; Schlögl, R.; Ertl, G. *Journal of Catalysis* **1992,** 138, (2), 413-444.
3. Easterday, R.; Sanchez-Felix, O.; Stein, B. D.; Morgan, D. G.; Maren, P.; Losovyj, Y.; Bronstein, L. M. *J. Phys. Chem. C* **2014,** 118, (42), 24769-24775.